Research Paper

3D-Resolved Investigation of the pH Gradient in Artificial Skin Constructs by Means of Fluorescence Lifetime Imaging

Raluca Niesner,[1,3] Bülent Peker,[1] Peter Schlüsche,[1] Karl-Heinz Gericke,[1] Christine Hoffmann,[2] Dagmar Hahne,[2] and Christel Müller-Goymann[2]

Purpose. The development of substitutes for the human skin, e.g., artificial skin constructs (ASCs), is of particular importance for pharmaceutical and dermatologic research because they represent economical test samples for the validation of new drugs. In this regard, it is essential for the skin substitutes to be reliable models of the genuine skin, i.e., to have similar morphology and functionality. Particularly important is the barrier function, i.e., the selective permeability of the skin, which is strongly related to the epidermal pH gradient. Because the pH significantly influences the permeation profile of ionizable drugs such as nonsteroidal anti-inflammatory drugs, it is of major importance to quantitatively measure the epidermal pH gradient of the ASC and compare it to that of genuine skin.

Methods. Using three-dimensional fluorescence lifetime imaging combined with two-photon scanning microscopy, we measured with submicron resolution the three-dimensional pH gradient in the epidermis of ASCs stained with 2′,7′-bis-(2-carboxyethyl)-5/6-carboxyfluorescein.

Results. Similar to genuine skin, the surface of the artificial epidermis has an acidic character (pH 5.9), whereas in the deeper layers the pH increases up to 7.0. Moreover, the pH gradient differs in the cell interior (maximally 7.2) and in the intercellular matrix (maximally 6.6). Apart from the similitude of the pH distribution, the genuine and the artificial skin prove to have similar morphologies and to be characterized by similar distributions of the refractive index.

Conclusions. Artificial skin is a reliable model of genuine human skin, e.g., in permeability studies, because it is characterized by a similar pH gradient, a similar morphology, and a similar distribution of the refractive index to that of genuine skin.

KEY WORDS: artificial skin constructs; barrier function; epidermal pH gradient; fluorescence lifetime imaging.

INTRODUCTION

Research and development of novel drugs for (trans) dermal administration require, among others, the testing of percutaneous penetration of the drug molecules across human skin. Before *in vivo* experiments, *in vitro* studies with excised human skin—or as a less appropriate alternative, with excised animal skin—have to be performed. Because excised animal skin is an insufficient substitute of human skin due to species variations in morphology and functionality; i.e., concerning drug permeability, excised human skin is preferred, although its resources are rather limited. Therefore, the development of human skin models that have the same properties (morphology and functionality) as genuine human skin is of particular significance (1,2). Very promising skin models are the three-dimensional (3D) artificial skin constructs (ASCs), which, similar to genuine skin, consist of an epidermis of differentiated keratinocytes and a dermis.

In the following, we will focus our attention on the barrier function of the skin, i.e., its selective permeability, with respect to the delivery of ionizable drugs. To the class of ionizable drugs belong nonsteroidal anti-inflammatory drugs, such as ibuprofen and diclofenac, and local anesthetics, such as lidocaine. These substances are weak acids or bases and can occur in the ionized and un-ionized form depending on the pH of the surrounding medium. Whereas the ionized form usually reveals a high solubility in aqueous media and, thus, a sufficiently high concentration gradient for a corresponding diffusion rate, the un-ionized form can freely diffuse in lipophilic media. The barrier function of the skin is mainly determined by the upper lipophilic layers of the epidermis, i.e., stratum corneum. Moreover, the acidic mantle of the skin is responsible for low values of pH on the skin surface. Thereby, a pH gradient of a few pH units exists between the outer stratum corneum layers and the viable part of the epidermis characterized by a physiological pH. Both factors influence the permeation profile of the ionizable drugs through the skin (3–6). As far as the pH

[1] Institute for Physical and Theoretical Chemistry, Technical University, Braunschweig, Germany.
[2] Institute for Pharmaceutical Technology, Technical University, Braunschweig, Germany.
[3] To whom correspondence should be addressed. (e-mail: raluca. niesner@tu-braunschweig.de)

gradient is concerned, it was shown that a modification of the pH of the epidermis results in a modification of the ionization state of the drugs and, thus, in a modification of the permeation profile (3,5,6). Consequently, to demonstrate the reliability of the ASCs as models of the genuine human skin in permeability studies, it is necessary to compare their pH gradient with that of genuine skin.

Because the 3D spatial distribution of the pH is needed, bulk pH experiments, which allow only the measurement of an average pH value at the skin surface, are evidently not appropriate. An alternative technique, which allows the measurement of the pH as a function of epidermal depth using a flat electrode, is based on tape stripping (7). The main drawback of this procedure is that it is intrinsically destructive and, thus, the natural function of the tissue is disturbed. Furthermore, it has a poor lateral resolution (in the centimeter range), so that no subcellular measurement of the pH is possible within a depth layer (7).

To visualize the skin with high 3D resolution and without damaging it, different microscopy techniques have been developed, e.g., tandem scanning microscopy (8), confocal scanning microscopy, and two-photon scanning microscopy (TPM) (9–12). Due to its advantages, i.e., noninvasive, excellent intrinsic 3D resolution, large penetration depth, low photo damage in the out-of-focus region, and simple experimental setup, TPM has proven to be the optimal method in the 3D-resolved imaging of thick biological samples including skin and ASCs (13–15).

In standard TPM experiments, the fluorescence intensity emitted by the sample is registered. If the skin samples are stained with an appropriate indicator for which the fluorescence spectrum varies with the pH, the spatial distribution of the pH in the epidermis can be determined. However, because the fluorescence intensity of the sample is strongly affected by experimental factors, e.g., modifications of the laser power and wavelength or variations of the chromophore concentration, and not only by the pH, such fluorimetric experiments lead to inaccurate results.

Fluorescence lifetime imaging (FLIM) is a versatile alternative to fluorimetric techniques due to its remarkable instrumental stability. In this case, the parameter, which depends on the pH, is the fluorescence lifetime of the staining chromophore and not its fluorescence wavelength. This time-dependent parameter of the fluorescence signal is scarcely perturbed by experimental factors, but for certain substances, e.g., BCECF, SNARF, or SNAFL, it is very sensitive to the pH value (16). FLIM experiments have been performed to monitor the pH gradient in the stratum corneum of mouse skin (7,17).

Moreover, FLIM found large application in the investigation of other cellular parameters, e.g., ion and oxygen concentration and viscosity (18–21), and in the elucidation of vital processes like cell metabolism, photosynthesis of green plants, or fluorescence resonance energy transfer (FRET) (18,19,22–25). To the principal methods of measuring the fluorescence decay time in an image belong frequency-domain techniques (7,16,18,21,22,26–28) and time-domain techniques, e.g., time correlated single-photon counting (TCSPC) (19,29) and time-gated procedures (23–25).

In conclusion, FLIM combined with TPM is the optimal technique to monitor the pH gradient in artificial epidermis with a subcellular 3D resolution and without damaging the samples. Although very important in the characterization of the barrier function of the ASC, to our knowledge, no such investigation of the artificial skin has been performed yet.

We used time-domain FLIM combined with TPM to obtain the 3D distribution of the pH in the epidermis of the ASC stained with BCECF. Thereby, the samples were neither photodamaged nor mechanically damaged.

To assure a high accuracy in the determination of the pH, we took into consideration that the fluorescence lifetime of BCECF may also be influenced by other factors than the pH such as refractive index n, viscosity η, or ion concentration. Whereas the influence of viscosity and ion concentration on the fluorescence lifetime of BCECF is negligible, the fluorescence lifetime is inversely proportional to the squared refractive index n^2. Therefore, a correction of the fluorescence lifetime images of the BCECF-stained ASC for the refractive index n is necessary; thus, it is essential to determine the n gradient in the heterogeneous artificial epidermis. In FLIM experiments on ASC stained with coumarin 314, we determined the local refractive index of the artificial epidermis with high 3D resolution. This local refractive index was used to correct the fluorescence lifetime images of BCECF-stained samples before converting them into pH images. To our knowledge, it is the first time that an epidermal n gradient is obtained by means of FLIM and that the fluorescence lifetime images of BCECF-stained samples are corrected for a local, i.e., not averaged (7), refractive index before converting them into pH images.

The 3D representation of the pH in the artificial epidermis revealed that the pH at the surface is acidic (5.9) and it increases with increasing depth. At the junction between the stratum corneum and stratum granulosum, a neutral pH was measured. Furthermore, we observed that the pH gradient in the cell interior and in the intercellular matrix, respectively, differed significantly.

By comparing the pH distribution, the n distribution, and the morphology of the ASCs with data obtained for genuine human skin, we can conclude that the ASCs are very reliable yet simplified skin models.

MATERIALS AND METHODS

Artificial Skin Constructs

The ASCs consist of a collagen matrix with incorporated human dermal fibroblasts, i.e., the artificial dermis, covered by an epidermis equivalent of differentiated human adult at low calcium concentration and elevated temperature (HaCaT) keratinocytes (1). They were cultivated as described by Specht *et al.* with a final modification by Wasserman and Müller-Goymann (1,2).

For imaging experiments, the ASCs were stained with 50 μmol L^{-1} buffer solutions (pH 7.15) of coumarin 314 (C314) and 2′,7′-bis-(2-carboxyethyl)-5/6-carboxyfluorescein (BCECF), respectively. Thereby, 2 mL of fluorophore solution was mixed in the growing medium of the skin constructs. Rapid staining of the ASC was attained by supplementary addition of about 50 μL DMSO. The staining process typically lasted approx. 30 min. During this period, a sufficient con-

centration of chromophore was assimilated by the samples. To avoid damages of the ASC, all experiments were performed within 2 h after removing them from the incubator.

Coumarin 314 (Lambda Physik, Göttingen, Germany), BCECF (Fluka, Buchs, Switzerland), DMSO p.a., and buffer solutions of different pH (Merck, Darmstadt, Germany) were used without further purification. Neither C314 nor BCECF had a cytotoxic effect on the ASCs.

Methods

TPM is a noninvasive imaging technique very suitable for the 3D-resolved investigation of the morphology of thick, highly scattering samples, e.g., the ASCs (9,10,14). By combining this technique with FLIM, new insight into the functionality of the samples can be obtained, i.e., environmental parameters, such as pH, refractive index n, viscosity η, or ion concentration as well as vital cellular processes can accurately be monitored with high 3D resolution (19–21).

Two-Photon Scanning Microscopy

In typical TPM experiments, a pulsed laser beam is focused by a high-aperture microscope objective into the sample. The fluorophore molecules of the sample, which dwell in a 3D-confined region around the focus (in the excitation volume), are simultaneously excited by two near-infrared (NIR, 700–1000 nm) laser photons and consequently fluoresce. The emitted fluorescence is registered to obtain information about the morphology of the studied sample (13). The secondary and principal axes (ω_0 and z_R) of the elliptical excitation volume indicate the spatial resolution at the x–y plane perpendicular to the optical axis and in the z direction, on the optical axis, respectively (31). Hereby, the diffraction-limited point spread function, i.e., the unitless laser intensity distribution, is approximated by a 2D Gauss–Lorentz distribution (13,30).

In contrast to confocal one-photon experiments, in TPM the excitation succeeds almost exclusively with ballistic photons, i.e., no scattered photons (32). Moreover, the NIR light typically used in TPM is less absorbed by biological tissues than the UV light used in one-photon experiments (13,30,32). Thus, in TPM experiments diffraction-limited resolution and an excellent signal-to-background ratio are maintained down to about 200-µm depth in tissue and neither photodamage nor photobleaching of the sample occur outside the focal plane.

To rapidly achieve information about the morphology of ASCs, we employed scanning TPM. In this way, fast optical sectioning was possible with a large 3D resolution and without any mechanical injury to the sample.

Fluorescence Lifetime Imaging

The fluorescence signal of molecules is characterized not only by intensity and wavelength but also by time-dependent properties, e.g., fluorescence lifetime τ. The fluorescence lifetime of both exogenous and endogenous chromophores is a valuable parameter for biological investigations because not only is it scarcely affected by experimental factors like chromophore concentration or fluctuations of the laser power, but it is also very sensitive to environmental parameters like pH, refractive index n, or ion concentration (19).

The fluorescence lifetime τ can be determined either in frequency-domain or in time-domain experiments (20). In frequency domain, τ is calculated from the phase difference between the modulated laser beam and the fluorescence signal. Time-domain techniques are more direct and simple procedures to obtain the fluorescence lifetime because therein the fluorescence lifetime τ is determined as a parameter of the experimentally measured fluorescence intensity decay, i.e., an exponential time decay (19).

By combining the fluorescence lifetime measurement with imaging techniques (FLIM), one can obtain a highly resolved spatial distribution of the fluorescence lifetime, and, thus, the heterogeneous distribution of the corresponding environmental parameter at the sample can be monitored. In our experiments, we used time-domain FLIM based on a time-gated technique due to its advantages, i.e., instrumental stability, rapid registration of the data, and simple evaluation (23–25).

Hereby, a series of fluorescence intensity images is registered at subsequent moments t after the laser pulse; thus, in each pixel of the image a fluorescence decay curve is recorded. Because from each decay curve, a fluorescence lifetime can be determined, a fluorescence lifetime image (τ map) of the same dimensions as the initial fluorescence intensity image is generated. This procedure can be repeated for different z positions in the sample, and a 3D-resolved representation of the fluorescence lifetime and of the corresponding environmental parameter is obtained.

Experimental Setup

The basic setup of the two-photon microscope used in our experiments is similar to setups previously described (14). The characteristics of the pulsed laser beam of the Ti:Sa laser (Mira 900, Coherent, Palo Alto, CA, USA) are 200-fs pulse width, 76-MHz repetition rate, and 169-nJ pulse energy. The laser beam is driven by two galvanometric mirrors (GSI Lumonics, Unterschleissheim, Germany) to scan the sample in the x–y plane. In the z direction, the sample is driven by a piezoelectric stage (Physik Instrumente, Waldbronn, Germany) with a precision of 8.42 nm. A Carl Zeiss (Jena, Germany) microscope objective Achroplan (63×, NA = 0.95, water immersion) is used to focus the 10-fold extended laser beam into the sample. The dimensions of the effective two-photon excitation volume (i.e., the resolution of the microscope) are, for a wavelength $\lambda = 830$ nm, $\omega_0 = 0.32$ µm in the x–y plane and $z_e = 1.35$ µm on the optical axis. The calibration was performed by means of fluorescent latex microbeads for the x–y resolution and of fluorescein–isothiocyanide monolayers for the z resolution (33). The fluorescence of the sample is collected by the same microscope objective and filtered by a dichroic mirror and by a band-pass filter (BG39, Schott).

As detection unit we used a time-gated system (LaVision, Göttingen, Germany) including a high repetition rate intensifier (HRI) with an adjustable gate (200–1,000 ps) combined with a CCD camera (480 × 640 pixels). The jitter of the detection system is less than 10 ps (8–9 ps measured in almost noise-free FLIM experiments) at a gate width of 200 ps. A

pixel on the CCD chip corresponds to 0.145 ± 0.05 μm in the sample. The dwell time of the laser beam per pixel during one scan is 0.95 μs. The size of the scanned field was 49 × 54 and 50 × 51 μm². Twenty-one fluorescence intensity images (3 s per frame) were registered at subsequent delays after the pulse in steps of 200 ps to generate the τ images.

The mean laser power at the sample was less than 3 mW, which ensures that neither functional nor morphological modifications of the tissue occur under NIR photo stress (14,24). Under these experimental conditions, the autofluorescence background of the ASC amounts to less than 0.1% of the registered signal.

RESULTS AND DISCUSSION

Two-Photon Scanning Microscopy in Artificial Skin Constructs

The advantages of TPM, i.e., reduced photo damage and no mechanical injury of the sample coupled with a high 3D resolution and a large penetration depth, have already been demonstrated on mouse and human skin (9–12). In this section, we control the applicability of TPM in the investigation of ASCs. Moreover, by comparing the morphology of the ASC with that of human skin, we verify the suitability of artificial skin as a model for genuine human skin.

We succeed in imaging the main segments of the ASC, i.e., epidermis and dermis, by employing TPM. The maximal penetration depth, i.e., the depth in the intact ASC, at which fluorescing structures can still be visualized, was about 170 μm.

In the artificial epidermis, three layers of differentiated keratinocytes/corneocytes could be identified. Starting from the surface, the corneocytes correspond to the stratum cor-

neum (thickness 8–10 μm), whereas the keratinocytes correspond to the stratum granulosum/spinosum (thickness 15–20 μm) and stratum basale (thickness 5–8 μm). The dimension of the keratinocytes is 5–7 μm in the stratum basale and 8–10 μm in the stratum granulosum/spinosum. The dimension of the corneocytes amounts to 12–15 μm in the stratum corneum (see Fig. 1). In the human skin, the dimension of the corneocytes amounts to 25–30 μm in the stratum corneum, whereas that of the keratinocytes amounts to 10–15 μm in the stratum granulosum/spinosum and approximately 7 μm in the stratum basale (excised from the abdominal region of a female donor, age 45 years). The thickness of the human epidermis varies between 50 μm on the eyelids and 1.5 mm on the palms and soles (10). Thus, the artificial and the excised human epidermis have similar morphologies, but the epidermal strata in the ASC are less developed as compared to those in human skin.

The artificial dermis consists of a matrix of collagen fibers with incorporated human dermal fibroblasts (see   Fig. 1). The collagen fibers are 3–5 μm thick whereas the fibroblasts are 25–30 μm long and have a maximal cross section of 15 μm. Although the morphology of the human dermis is more complex than that of the artificial dermis (8,10–12), the main dermal structures are met in both the artificial and the human skin. Thus, as far as the morphology is concerned, the ASCs are simplified yet reliable models of genuine human skin.
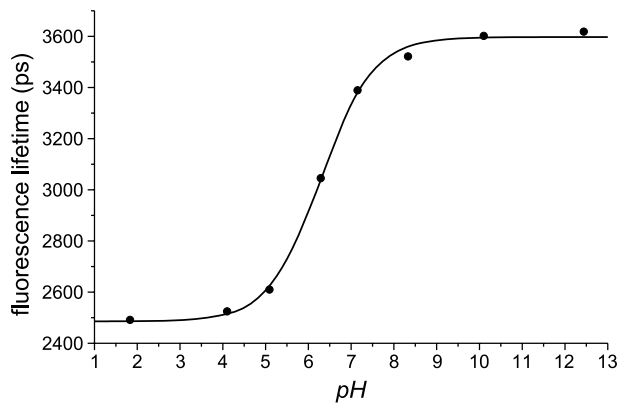
Fluorescence Lifetime Imaging in Artificial Skin Constructs

TPM enabled a detailed study of the morphology of the ASC. However, no information about the pH gradient of the artificial epidermis could be achieved.

TPM-FLIM experiments on skin constructs stained with BCECF first allowed the investigation of the pH gradient of
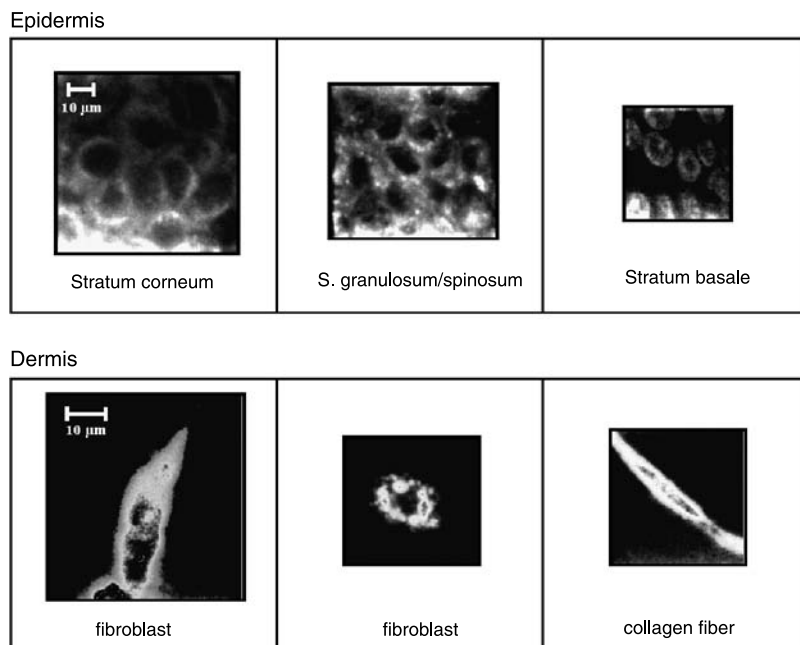
Fig. 1. TPM fluorescence intensity images of different layers in the artificial skin constructs stained with C314 or rhodamine B. The images of the epidermal layers were taken in 7, 14, and 30 μm depth, whereas dermal structures were visualized in 50–70 μm depth.

Fig. 2. Dependence of the fluorescence lifetime τ of BCECF (pH indicator) on the pH. The calibration was performed with aqueous buffer solutions of BCECF (refractive index $n = 1.33$).

the artificial epidermis with subcellular resolution and without damaging the samples. BCECF was selected as the pH indicator in the FLIM experiments because its fluorescence lifetime strongly depends on the pH. At acidic pH (pH ∼2) BCECF is protonated (HBCECF), whereas at basic pH (pH ∼12) it is unprotonated (BCECF⁻). The fluorescence lifetimes of the protonated and unprotonated species differ significantly (16). At pH values between these two extremes, both HBCECF and BCBCF⁻ are present in solution, contribute to the fluorescence signal, and thus influence the fluorescence lifetime. Especially for biological investigations, BCECF is the ideal pH indicator because its pK_a amounts to 7.0 and it is harmless to tissues.

We measured the dependence of the fluorescence lifetime of eight BCECF buffer solutions of pH between 1.83 and 12.44 to generate a calibration curve that will be used later to convert the τ images of the epidermal layers into pH images (see Fig. 2). At pH 1.83, at which only HBCECF is present in the solution, τ amounts to 2491 ± 20 ps, whereas at pH 12.44, at which BCECF is completely unprotonated (only BCBCF⁻), τ amounts to 3621 ± 17 ps. In the pH range of interest, i.e., between pH 4 and 8, the fluorescence lifetime of BCECF varies between 2524 ± 22 and 3521 ± 15 ps (1,000 ps dynamic range). The fluorescence lifetimes were determined in monoexponential FLIM experiments on buffer solutions of

BCECF. The standard deviation of about 20 ps in the determination of the fluorescence lifetime corresponds to an uncertainty of the pH determination of less than 0.05 pH units.

The calibration curve τ(pH) (Fig. 2) by itself does not allow an accurate conversion of the τ images of the epidermal layers into pH images because the fluorescence lifetime of BCECF may also be influenced by other factors, i.e., refractive index, viscosity, and ionic concentration, which are expected to be different in aqueous solution and in the artificial skin samples. We observed that the fluorescence lifetime of BCECF depends neither on the viscosity nor on the ion concentration (data not shown). As far as the dependence of the fluorescence lifetime τ on the refractive index n is concerned, it has been demonstrated that Eq. (1) is valid for all substances with a high fluorescence quantum yield, including BCECF (34).

$$\tau^{-1} = 2.88 \times 10^{-9} \times n^2 \int \varepsilon \frac{(2v_0 - v)^2}{v} dv. \tag{1}$$

Here, ε is the extinction coefficient at the frequency v and v_0 is equivalent to the frequency of the ground state to the first singlet-state transition.

To accurately convert τ images into pH images by means of the calibration curve τ(pH), the τ images must first be corrected for the corresponding refractive index. Thus, the determination of the n gradient in the artificial epidermis is essential. For this purpose, FLIM experiments in ASC stained with C314 were performed. Coumarin 314 is an adequate n indicator because its fluorescence lifetime is influenced only by the refractive index (data not shown). The fluorescence lifetime of C314 in aqueous solution ($n = 1.33$) was 3453 ± 15 ps.

From Eq. (1), the fluorescence lifetime τ scales inversely proportional to the square of the refractive index n. Using this relation, τ images of the artificial epidermis stained with C314 were converted into n images as shown in Fig. 3. In this way, the 3D gradient of the refractive index n in the artificial epidermis was ascertained.

The τ images of the artificial epidermis stained with BCECF can now be corrected for the corresponding refractive index and directly converted into pH images using the calibration curve τ(pH) (Fig. 2) as shown in Fig. 4. Thus, the

τ-map n-map
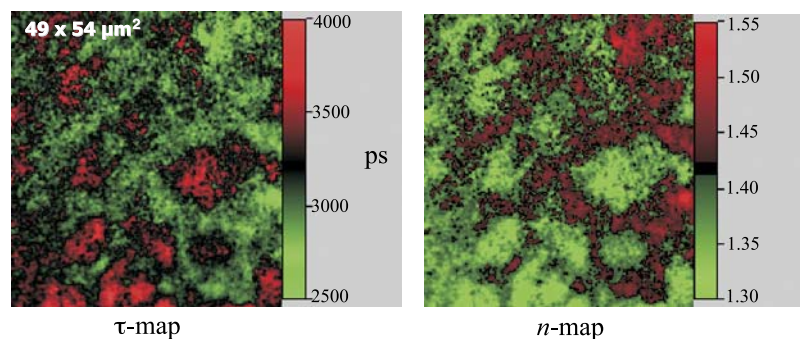
Fig. 3. Fluorescence lifetime image (τ map) and corresponding refractive index image (n map) of an epidermal layer (depth = 3.7 μm) in stratum corneum. The refractive index in the cell interior ($n = 1.34$) is significantly smaller than in the intercellular matrix ($n = 1.47$) due to a larger lipid content of the latter. The artificial skin sample was stained with an aqueous solution of C314 (50 μmol L⁻¹).

49 x 54 µm²

ps

τ-map   pH-map
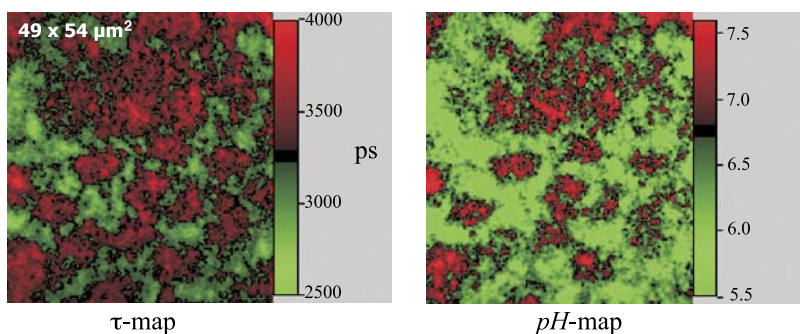
Fig. 4. Fluorescence lifetime image (τ map) corrected for *n* and corresponding pH image (pH map) of an epidermal layer (depth = 13.48 µm) in the stratum granulosum/ spinosum. The pH in the cell interior (pH 7.2 ± 0.1) is significantly larger than in the intercellular matrix (pH 6.3 ± 0.2). The artificial skin sample was stained with a 50-µmol L^{-1} buffer solution (pH 7.15) of BCECF.

exact 3D distribution of the pH in the artificial epidermis is obtained.

The correction of τ images of samples stained with BCECF for the refractive index *n* has already been applied by other scientists to convert τ images into pH images (1,2). However, this correction was not accurately performed because a refractive index averaged over the whole sample was used. To our knowledge, we determined for the first time a 3D *n* gradient by means of FLIM and corrected the τ images with the corresponding refractive index to accurately convert τ images into pH images.

n Imaging

Fluorescence lifetime images (τ maps) of 13 equidistant epidermal layers were generated down to 40 µm depth in the epidermis of artificial skin samples stained with C314. Using Eq. (1), we converted these τ maps into *n* images as described in the previous section.

In the upper layers (0–10 µm), i.e., stratum corneum, the refractive index of the cells is clearly smaller (*n* = 1.34 ± 0.01) than that of the intercellular matrix (*n* between 1.48 and 1.38) due to the higher lipid content of the latter (Fig. 3). At the surface (*z* = 0 µm) the lipid matrix dominates the cell interior and this results in a uniform distribution of the refractive index (*n* = 1.48 ± 0.01). In the deeper layers, i.e., beyond the junction between the stratum corneum and the stratum granulosum, there are no noticeable differences between the cell interior and the intercellular matrix as far as the refractive index is concerned (*n* = 1.35 ± 0.01) because both the cell interior and the intercellular matrix consist mostly of water.

Figure 5 provides an overview of the dependence of the refractive index *n* on the *z* position of the epidermal layer, whereby the refractive index was averaged over the 49 × 54-µm² *n* image. In the stratum corneum (0–10 µm) the decreasing lipid content induces a decrease of the averaged refractive index from 1.48 ± 0.01 to 1.37 ± 0.02. In the deeper layers (below 12 µm) the averaged refractive index reaches a constant value of 1.35 ± 0.01, which is slightly larger than that of water (*n* = 1.33).

Different methods, e.g., confocal Raman microspectroscopy or bifocal optical coherence refractometry, were employed to determine the refractive index distribution in the epidermis of human skin (35–37). In the stratum corneum,

the refractive index *n* varies between 1.6 and 1.37 depending on body site and sex, and it is maximal at the surface and minimal at the junction between the stratum corneum and granulosum (35–37). In the deeper strata, the refractive index *n* is a constant slightly larger than that of water (35–37). In conclusion, as far as the refractive index is concerned, the ASCs are very similar to genuine human skin.

In the following, the results obtained in the FLIM experiments in ASC stained with C314 will be used to correctly convert the fluorescence lifetime images of the artificial epidermis stained with BCECF into pH images.

pH Imaging

Because the molecular transport of ionizable compounds is closely connected to the pH of the surrounding tissue and, thus, to the barrier function of the artificial epidermis, investigation of the 3D pH gradient in the epidermal strata is essential to demonstrate the applicability of ASCs as models of genuine human skin in permeability studies. Therefore, in FLIM experiments on artificial skin samples stained with
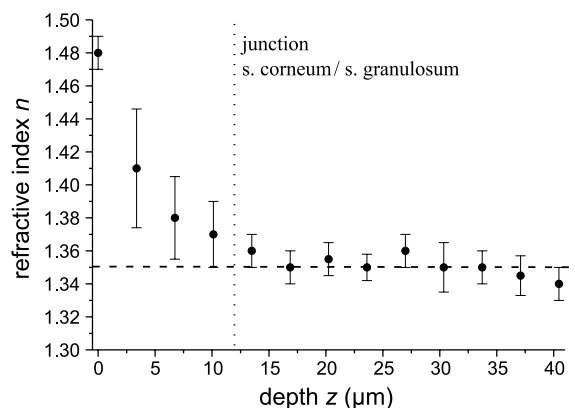
Fig. 5. Dependence of the refractive index *n* on the *z* position of the epidermal layer in ASC stained with C314. The refractive index was integrated over a 49 × 54-µm² *n* image. The error bars represent the variation of the refractive index within an image. They are very large in the stratum corneum because the differences between *n* in the cell interior and in the intercellular matrix are also very large. As expected, the error bars are small beyond the junction between the stratum corneum and stratum granulosum (below 12 µm).
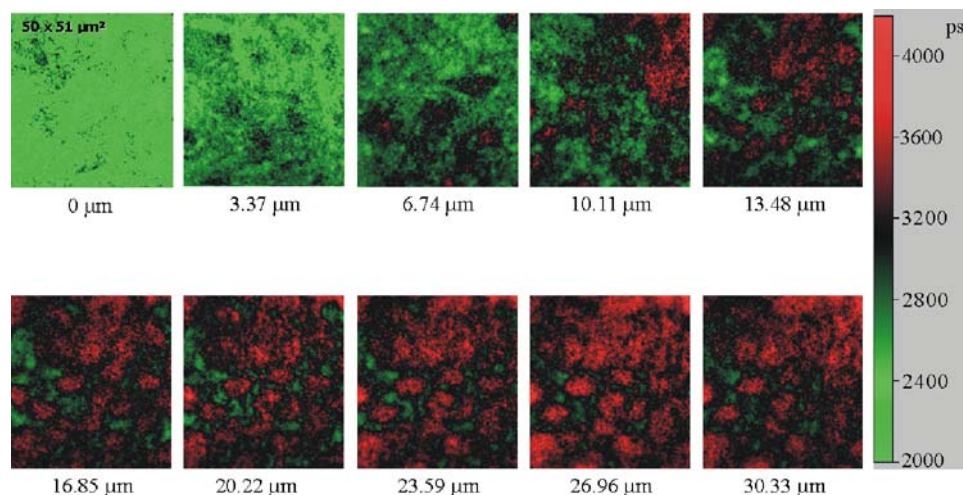
Fig. 6. Dependence of the fluorescence lifetime τ of BCECF on the z position of the epidermal layer. Because the fluorescence lifetime of BCECF increases with increasing pH, this series of images emphasizes once more the 3D pH gradient in the artificial epidermis. The z position is denoted under each image.

BCECF, τ images of 14 epidermal layers were generated down to 30-μm depth.

Figure 6 shows fluorescence lifetime maps of epidermal layers in BCECF-stained ASCs in ten different depths z. Because the fluorescence lifetime of BCECF increases with increasing pH (Fig. 2), these images represent a first qualitative 3D visualization of the epidermal pH gradient. To quantitatively visualize the epidermal pH gradient, the τ images were first corrected for the corresponding refractive index n and then converted into pH images as previously described.

Differences between the pH of the cell interior (between 6.0 and 7.2) and of the intercellular matrix (between 5.8 and 6.6) are observed all throughout the artificial epidermis. As shown in Fig. 4, the pH of the cell interior in 13.48-μm depth amounts to 7.2 ± 0.1 (averaged over six cells), whereas the pH of the intercellular matrix is 6.3 ± 0.2 (averaged over seven regions). Only at the surface ($z = 0$ μm), both the cells and the intercellular matrix are characterized by the same acidic pH of 5.9 ± 0.1.
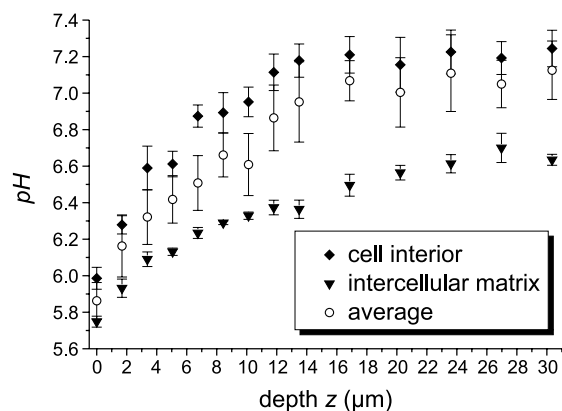
Fig. 7. Dependence of the pH on the z position of the epidermal layer in ASC stained with BCECF. Error bars represent the variation of the pH in the cell interior, the intercellular matrix, and within the 49×54-μm² pH image. In all the cases, the pH increases with increasing depth z.

In Fig. 7 the dependence of the pH on the z position of the epidermal layer is schematically plotted. The pH of the cell interior rapidly increases in the stratum corneum (0 to 10 μm) from 6.0 to 7.2 and remains constant (pH 7.2) in the deeper layers beyond the junction between the stratum corneum and granulosum (less than 12 μm). An increasing tendency shows also the pH of the intercellular matrix. However, in this case the pH increases all throughout the epidermis (depth z between 0 and 30 μm) and does not exceed a value of 6.6 ± 0.1. Qualitatively, the profile of the pH averaged over a pH image is similar to the pH gradients in the cell interior and in the intercellular matrix, respectively (Fig. 7).

Previous pH measurements revealed that the stratum corneum of genuine human skin has an acidic pH, which is minimal at the surface and increases with depth (7,17). The pH at the surface of stratum corneum ranges between 4.5 and 6.0 depending on body site, sex, and species (7). Furthermore, it was shown that the pH of the viable epidermis is neutral (7.0), whereas that of the viable cells is approximately 7.2 (7,17). Thus, we can conclude that ASCs have a similar pH gradient as the genuine human skin, supporting the usefulness of ASCs in permeability studies. A 3D pH gradient in the human epidermis, which would allow an accurate comparison of the genuine tissue with the artificial one, has not been measured yet.

pH measurements similar to ours have been performed by means of FLIM on mouse skin samples. However, these experiments are not reliable because in the evaluation of the pH images, the value of the refractive index was considered to be 1.38 throughout the epidermis, i.e., the differences in refractive index between the cell interior and intercellular matrix and between the different depth positions of the epidermal layers, respectively, were completely neglected.

CONCLUSIONS

We studied for the first time in detail the pH gradient of the epidermis of ASCs by means of FLIM combined with

TPM. Such an investigation is of particular significance because the epidermal pH gradient plays a central role in the transport of ionizable molecules across the skin, i.e., selective permeability of the skin. As pointed out, if the pH gradient of the ASC is different from that of genuine skin, major differences in the permeation profiles of ionizable drugs would be expected. Thus, by comparing the pH gradient in the artificial and genuine epidermis, assertions about the reliability of the ASCs as human skin models in permeability studies are for the first time possible.

In FLIM experiments on ASCs stained with BCECF, a 3D representation of the epidermal pH was obtained, which revealed that, similar to the genuine skin, the surface of the artificial epidermis has an acidic character (pH 5.9). Moreover, the pH rapidly increases in the stratum corneum up to neutral pH (7.0) and remains constant in the deeper epidermal layers. We have also observed that the pH increase in the stratum corneum is more pronounced in the cell interior than in the intercellular matrix. Beyond the junction between the stratum corneum and granulosum, the pH of the cell interior remains constant (pH 7.2), whereas the pH of the intercellular matrix continues to increase but does not exceed a value of 6.6. These results lead to the conclusion that, as far as the pH gradient is concerned, the ASC and the genuine human skin are similar yet not identical; thus, the ASCs are reliable skin models for permeability experiments. Furthermore, the results of experiments in which the morphology and the refractive index gradient of the artificial epidermis were studied validate the eligibility of the ASCs as skin models.

ACKNOWLEDGMENT

REFERENCES

1. C. Specht, I. Stoye, and C. C. Müller-Goymann. Comparative investigations to evaluate the use of organotypic cultures of transformed and native dermal and epidermal cells for permeations studies. *Eur. J. Pharm. Biopharm.* **46**:273–278 (1998).
2. K. Wasserman and C. C. Müller-Goymann. Standardized cultivation of artificial skin constructs for drug permeation studies. *Arch. Pharm. Pharm. Med. Chem.* **333** (Suppl 1):34 (2000) (Abstract).
3. J. Hadgraft and C. Valenta. pH, pK(a) and dermal delivery. *Int. J. Pharm.* **200**:243–247 (2000).
4. Y. N. Kalia, F. Pirot, R. O. Potts, and R. H. Guy. Ion mobility across human stratum corneum *in vivo*. *J. Pharm. Sci.* **87**:1508–1511 (1998).
5. J. C. Smith and W. J. Irwin. Ionisation and the effect of absorption enhancers on transport of salicylic acid through rubber and human skin. *Int. J. Pharm.* **210**:69–82 (2000).
6. D. Marro, R. H. Guy, and M. B. Delgado-Charro. Characterisation of the iontophoretic permselectivity properties of human and pig skin. *J. Control. Rel.* **70**:213–217 (2001).
7. K. M. Hanson, M. J. Behne, N. P. Barry, T. M. Mauro, E. Gratton, and R. M. Clegg. Two-photon fluorescence lifetime imaging of the skin stratum corneum pH gradient. *Biophys. J.* **83**:1682–1690 (2002).
8. P. Corcuff and J.-L. Lévêque. *In vivo* vision of the human skin with the tandem scanning microscope. *Dermatology* **186**:50–54 (1993).
9. B. R. Masters, P. T. C. So, and E. Gratton. Multiphoton excitation microscopy of *in vivo* human skin. Functional and morphological optical biopsy based on three-dimensional imaging, lifetime measurements and fluorescence spectroscopy. *Ann. N.Y. Acad. Sci.* **838**:58–67 (1998).
10. B. R. Masters, P. T. C. So, and E. Gratton. Multiphoton excitation fluorescence microscopy and spectroscopy of *in vivo* human skin. *Biophys. J.* **72**:2405–2412 (1998).
11. K. König, U. Wollina, I. Riemann, C. Peuckert, K.-J. Halbhuber, H. Konrad, P. Fischer, V. Fünfstück, T. Fischer, and P. Elsner. Optical tomography of human skin with subcellular spatial and picosecond time resolution using intense near infrared femtosecond laser pulses. *SPIE* **4620**:191–201 (2002).
12. P. T. C. So, H. Kim, and I. E. Kochevar. Two-photon deep tissue *ex vivo* imaging of mouse dermal and subcutaneous structures. *Opt. Express* **3**:339–350 (1998).
13. W. Denk, J. H. Strickler, and W. W. Webb. Two-photon laser scanning fluorescence microscopy. *Science* **248**:73–76 (1990).
14. K. König. Multiphoton microscopy in life sciences. *J. Microsc.* **200**:83–104 (2000).
15. E. Gratton, N. P. Barry, S. Beretta, and A. Celli. Multiphoton fluorescence microscopy. *Methods* **25**:103–110 (2001).
16. H. Szmacinski and J. R. Lakowicz. Optical measurements of pH using fluorescence lifetimes and phase-modulation fluorimetry. *Anal. Chem.* **65**:1668–1674 (1993).
17. M. J. Behne, J. W. Meyer, K. M. Hanson, N. P. Barry, S. Murata, D. Crumrine, R. W. Clegg, E. Gratton, W. M. Holleran, P. M. Elias, and T. M. Mauro. NHE1 regulates the stratum corneum permeability barrier homeostasis. *J. Biol. Chem.* **277**:47399–47406 (2002).
18. J. R. Lakowicz and K. Berndt. Lifetime-selective fluorescence imaging using a rf phase-sensitive camera. *Rev. Sci. Instrum.* **62**:1727–1734 (1991).
19. W. Becker and A. Bergmann. Lifetime imaging techniques for optical microscopy. http://www.becker-hickl.de/pdf/tcvgbhl.pdf (2003).
20. A. Draaijer, R. Sanders, and H. C. Gerritsen. In J. Pawley (ed.), *Handbook of Biological Confocal Microscopy*, Plenum, New York, 1995, pp. 491–505.
21. J. R. Lakowicz, H. Szmacinski, and M. L. Johnson. Calcium imaging using fluorescence lifetimes and long-wavelength probes. *J. Fluoresc.* **2**:47–62 (1992).
22. S. Murata, P. Herman, and J. R. Lakowicz. Texture analysis of fluorescence lifetime images of nuclear DNA with effect of fluorescence resonance energy transfer. *Cytometry* **43**:94–100 (2001).
23. D. Elson, S. Webb, J. Siegel, K. Suhling, D. Davis, J. Lever, D. Phillips, A. Wallance, P. French, K. Lauritsen, M. Wahl, and R. Erdmann. Fluorescence lifetime system for microscopy and multiwell plate imaging with a blue picosecond diode laser. *Opt. Lett.* **27**:1409–1411 (2002).
24. R. Niesner, B. Peker, P. Schlüsche, and K.-H. Gericke. Noniterative biexponential fluorescence lifetime imaging in the investigation of cellular metabolism by means of NAD(P)H autofluorescence. *Chem. Phys. Chem.* **5**:1141–1149 (2004).
25. V. Barzda, C. J. Grauw, J. Vroom, F. J. Kleima, R. van Grondelle, H. van Amerongen, and H. C. Gerritsen. Fluorescence lifetime heterogeneity in aggregates of LHC II revealed by time-resolved microscopy. *Biophys. J.* **81**:538–546 (2001).
26. A. Squire, P. J. Verveer, and P. I. H. Bastiaens. Multiple frequency fluorescence lifetime imaging microscopy. *J. Microsc.* **197**:136–149 (2000).
27. P. J. Verveer, A. Squire, and P. I. H. Bastiaens. Global analysis of fluorescence lifetime imaging microscopy data. *Biophys. J.* **78**:2127–2137 (2000).
28. E. Gratton, S. Breusegem, J. Sutin, Q. Ruan, and N. Barry. Fluorescence lifetime imaging for two-photon microscope: time-domain and frequency-domain methods. *J. Biomed. Opt.* **8**:381–390 (2003).
29. W. Becker, A. Bergmann, C. Biskup, T. Zimmer, N. Klöcker, and K. Benndorf. High resolution TCSPC lifetime imaging. *Proc. SPIE* **4620** (2002).
30. X. Deng, X. Gan, and M. Gu. Multiphoton fluorescence microscopic imaging through double-layer turbid tissue media. *J. Appl. Phys.* **91**:4659–4665 (2002).

31. J. Mertz, C. Xu, and W. W. Webb. Single-molecule detection by two-photon-excited fluorescence. *Opt. Lett.* **20**:2532–2534 (1995).

32. H. Szmacinski, I. Gryczynski, and J. R. Lakowicz. Spatially localized ballistic two-photon excitation in scattering media. *Biospectroscopy* **4**:303–310 (1998).

33. A. Schönle, M. Glatz, and S. W. Hell. Four-dimensional multiphoton microscopy with time-correlated single-photon counting. *Appl. Opt.* **39**:6306–6311 (2000).

34. S. J. Strickler and R. A. Berg. Relationship between absorption intensity and fluorescence lifetime of molecules. *J. Chem. Phys.* **37**:814–822 (1962).

35. P. J. Caspers, G. W. Lucassen, E. A. Carter, H. A. Bruining, and G. J. Puppels. *In vivo* confocal Raman microspectroscopy of the skin: noninvasive determination of molecular concentration profiles. *J. Invest. Dermatol.* **116**:434–442 (2001).

36. A. V. Zvyagin, K. K. M. B. Dilusha Silva, S. A. Alexandrov, T. R. Hillman, and J. J. Armstrong. Refractive index tomography of turbid media by bifocal optical coherence refractometry. *Opt. Express* **25**:3503–3517 (2003).

37. S. A. Alexandrov, A. V. Zvyagin, K. K. M. B. Dilusha Silva, and D. D. Sampson. Bifocal optical coherence refractometry of turbid media. *Opt. Express* **2**:117–119 (2003).